Check for updates

Dye degradation and antimicrobial efficacy of cesium-doped Y₂O₃ nanostructures: *in silico* docking study†

Muhammad Ikram, [ID] *[ab] Yasir Shabir,[c] Ali Haider, [ID] *[d] Iram Shahzadi,[e] Muhammad Bilal,[a] Anwar Ul-Hamid, [ID] *[f] Ahmed M. Fouda[g] and Salamat Ali[h]

Developing multifunctional nanomaterials is crucial to rising global concerns over environmental contamination caused by dye effluents and antibiotic resistance. This work presents cesium (Cs)-doped Y₂O₃ nanostructures (NSs) as viable options for catalytic dye degradation and antibacterial action. This study prepared yttrium oxide (Y₂O₃) and various (2, 4, and 6 wt%) concentrations of Cs-doped Y₂O₃ NSs *via* co-precipitation technique. The pure and Cs-doped Y₂O₃ NSs were used to degrade methylene blue (MB) at different pH levels and assess the antibacterial properties against multidrug-resistant (MDR) *Escherichia coli* (*E. coli*). The X-ray diffraction spectra of the pure and Cs-doped Y₂O₃ revealed the presence of cubic and monoclinic structures. The UV-vis absorption spectra displayed distinct peaks at 274 nm and a reduction in band gap energy (from 4.94 eV to 4.41 eV) upon incorporation of Cs. Maximum degradation efficiency of up to 99% attributed to 6% Cs-doped Y₂O₃. The bactericidal activity against MDR *E. coli* exhibited 4.15 mm inhibition zones at higher concentrations of Cs-doped Y₂O₃. The bactericidal mechanism of Cs-Y₂O₃ NSs was further investigated by molecular docking studies for β-lactamase and DNA gyrase enzymes.

1. Introduction

Environmental health is seriously threatened by the increasing presence of organic pollutants and the rise of drug-resistant pathogens in wastewater systems. Numerous sectors, including leather, textile, plastic, and paper industries, regularly emit large amounts of pollutants that directly impact the environment.[1–3] According to the United Nations, more than 80% of wastewater is discharged into rivers without removing

Solar Cell Applications Research Lab, Department of Physics, Government College University Lahore, Lahore, 54000, Punjab, Pakistan. E-mail: dr.muhammadikram@gcu.edu.pk

Advance Nanomaterials Research Lab, Department of Physics, Government College University Lahore, Lahore, 54000, Punjab, Pakistan

Department of Physics, Riphah Institute of Computing and Applied Sciences (RICAS), Riphah International University, 14 Ali Road, Lahore, Pakistan

Department of Clinical Medicine, Faculty of Veterinary and Animal Sciences, Muhammad Nawaz Shareef, University of Agriculture, 66000, Multan, Punjab, Pakistan. E-mail: ali.haider@mnsuam.edu.pk

School of Pharmacy, University of Management and Technology, Lahore, 54770, Pakistan

Core Research Facilities, King Fahd University of Petroleum & Minerals, Dhahran, 31261, Saudi Arabia. E-mail: anwar@kfupm.edu.sa

Chemistry Department, Faculty of Science, King Khalid University, P. O. Box 9004, Abha, 61413, Saudi Arabia

Department of Physics, The University of Lahore, 54000, Pakistan

† Electronic supplementary information (ESI) available. See DOI: https://doi.org/10.1039/d4ra05620e

hazardous components.[4] Dyes in those industrial wastes have serious health and environmental issues, such as mutagenic and carcinogenic effects.[5,6] The presence of multidrug-resistant (MDR) bacterial species in those reservoirs seriously threatens public health. *Escherichia coli* (*E. coli*) is one of the diarrheagenic *E. coli* pathotypes that causes several deaths in children and is responsible for 1.3 million deaths annually.[7] Several conventional methods have had adopted to remove these contaminants from wastewater, including coagulation, biological treatment, evaporation, filtering, electrochemical, advanced oxidation process, adsorption, ion exchange, and photocatalysis.[8–11] These traditional wastewater treatment and antimicrobial intervention techniques frequently experience issues with sustainability, cost-effectiveness, and efficiency. Among these methods catalytic degradation has proved to degrade the dye pollutant more efficiently. Catalytic degradation based on nanomaterials is simple, cost-effective and has the benefit of being recyclable.[7] The development of multifunctional nanomaterials with both catalytic and antibacterial qualities is an unmet demand despite advances in nanotechnology.

The composition and structure of nanomaterials significantly impact most of their applications.[12–14] Rare earth elements have attracted much interest in pharmacology and medicine due to their antitumor, antibacterial, antiemetic, anticoagulant, and anticancer activities.[15] Yttrium oxide (Y₂O₃), one of the 17 rare earth oxides, exists in different cubic,

hexagonal, and monoclinic structural phases.[16–18] Modified Y_2O_3 can be a reliable option for developing multifunctional nanomaterials. Various techniques can be used to synthesize Y_2O_3 nanoparticles. For homogeneity and size control, the co-precipitation approach is discovered as an effective synthesis method.[19] For modification, the huge atom size of the cesium (Cs) as a doping element was anticipated to have considerable effects on adjusting the physical characteristics of materials.[20] The present study investigates the potential of Cs-doped Y_2O_3 NSs as a feasible solution to these important research areas. The objective is to produce a multipurpose material that can degrade organic contaminants and fight pathogens that are resistant to antibiotics by fusing the catalytic qualities of Y_2O_3 with the distinctive characteristics of cesium. The significance of this work stems from its ability to give an extended and effective solution to two major global concerns.

Using a co-precipitation approach, this study synthesized Y_2O_3 and various concentrations (2, 4 and 6 wt%) of Cs-doped Y_2O_3. The catalytic degradation of methylene blue (MB) dye and antibacterial efficacy against MDR *E. coli* were investigated to evaluate their potential. Moreover, *in silico* investigations for β-lactamase and DNA gyrase enzymes were also carried out to understand the underlying mechanisms of antibacterial activity.

2. Experimental part

2.1. Materials

Yttrium(III) nitrate hexahydrate $(Y(NO_3)_3 \cdot 6H_2O$, 99.8%) was purchased from Sigma-Aldrich USA. Cesium nitrate $(CsNO_3,$ 99%) and NaOH, 98% were obtained from Sigma-Aldrich, Germany.

2.2. Synthesis of pure and Cs-doped yttrium oxide

Y_2O_3 and 2, 4, and 6 wt% of Cs-doped Y_2O_3 were synthesized *via* co-precipitation. 0.1 M of $Y(NO_3)_3 \cdot 6H_2O$ was prepared as a source of Y under continuous stirring and heating *via* a hot-plate at 100 °C for 30 minutes. The precipitating agent NaOH (1 M) was incorporated dropwise to obtain the precipitates and maintain a pH of 10. The obtained precipitate was stirred for 2 hours at 150 °C to obtain a colloidal solution. The colloidal precipitates were centrifuged at 7500 rpm to remove impurities from the stirred solution after heating at 150 °C for 14 hours. The fine powder was achieved by grinding with mortar and pestle. Different concentrations of Cs (2, 4, and 6 wt%) were introduced as dopants into the prior precursor solution of $Y(NO_3)_3 \cdot 6H_2O$ to synthesize Cs-doped Y_2O_3. The schematic of the synthesized Cs-doped Y_2O_3 is represented (Fig. 1).

2.3. Catalytic activity

The catalytic potential of pure and Cs-doped Y_2O_3 NSs was evaluated through MB degradation (Fig. 2). The produced NSs serve as the catalysts and sodium borohydride $(NaBH_4)$ acts as a reducing agent. To ensure experimental purity, both MB and $NaBH_4$ solutions were prepared freshly. Subsequently, 400 μL of $NaBH_4$ was incorporated in aqueous MB solution (3 mL). Then, 400 μL of pure and Cs-doped Y_2O_3 nanocatalyst were added to the prior solution.

The catalyst enhanced the stability and reaction rate by decreasing the activation energy. MB was converted into lecuo methylene blue (LMB). The maximum absorption of MB occurs at 665 nm, which is used to measure the degradation of dye using UV-vis absorption spectroscopy. The percentage degradation of synthesized doped nanocatalyst was measured using eqn (1):

$$\% \text{ degradation} = (C_0 - C_t)/C_0 \times 100 \tag{1}$$

where the initial concentration (C_0) of MB and the final concentration (C_t) after incorporating NSs.

2.4. Isolation and identification of MDR *E. coli*

2.4.1. Isolation of *E. coli* bacteria. The unpasteurized milk has been collected from cows during various stages of lactation at many veterinary clinics in Punjab, Pakistan. The samples were promptly collected in aseptic glass receptacles and moved at 4 °C temperature under carefully monitored circumstances. The quantification of coliform pathogens in the unpasteurized milk samples has been performed using MacConkey agar. For 48 hours, the plates were incubated at 37 °C temperature.

2.4.2. Bacterial characterization and isolate identification. To identify *E. coli*, a series of tests including biochemical analysis, colony morphology examination, and Gram staining, were performed according to the protocols outlined in Bergey's Manual of Determinative Bacteriology.[21]

2.4.3. Antibiotic susceptibility. The antibiotic susceptibility was investigated using Mueller Hinton agar (MHA) *via* disc diffusion method.[22] *E. coli* bacteria was examined for antibiotic resistance to the following antibiotics (classes): ciprofloxacin (Cip) 5 μg (quinolones), tetracycline (Te) 30 μg (tetracyclines), amoxicillin (A) 30 μg (penicillins), gentamicin (Gm) 10 μg (aminoglycosides), imipenem (Imi) 10 μg (carbapenem), and azithromycin (Azm) 15 μg (macrolides). The investigation of *E. coli* strains exhibiting resistance to a 5 μg concentration of the ciprofloxacin antibiotic was carried out using a series of experimental procedures.[23] *E. coli* cultures were grown on Petri dish to achieve a turbidity level of 0.5 MacFarland standard. Subsequently, bacteria were evenly distributed over a medium known as MHA (Oxoid Limited, Basingstoke, United Kingdom). Antibiotic discs were placed on the inoculated plates at specific intervals to prevent inhibition zone interference. This action successfully prevented the disruption of inhibition zones. The plates were incubated for two days at specific temperature (37 °C) to cultivate bacteria. Subsequently, the collected data was analyzed using the Diagnostic, Therapeutic, and Laboratory Standard Institutes. At least three medications show ineffectiveness against MDR microorganisms.[24]

2.4.4. *In vitro* antibacterial activity. The agar well diffusion technique evaluated the potential bactericidal activity of pristine and Cs-doped Y_2O_3 NSs. Sterile swabs collected MDR *E. coli* bacteria colonies that were subsequently grown on Petri dishes. On MacConkey agar, the bacteria were cultivated at 0.5 McFarland standard. A sterile cork borer was used to create 6 mm diameter wells. The wells were filled with synthesized pure doped NSs at 0.5 mg/50 μL and 1.0 mg/50 μL, respectively. The concentration of ciprofloxacin (+ve control) was 0.005 mg/50 μL, whereas the
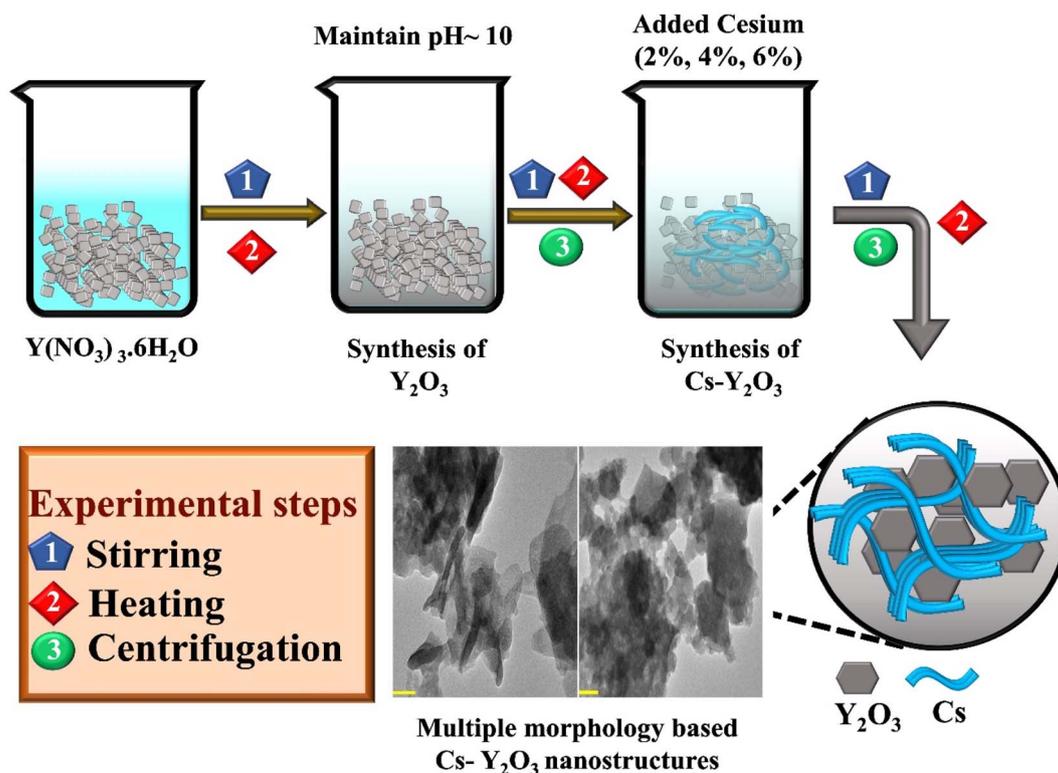
Fig. 1 Schematic showing the steps involved in synthesizing Cs-doped Y_2O_3 nanostructures.
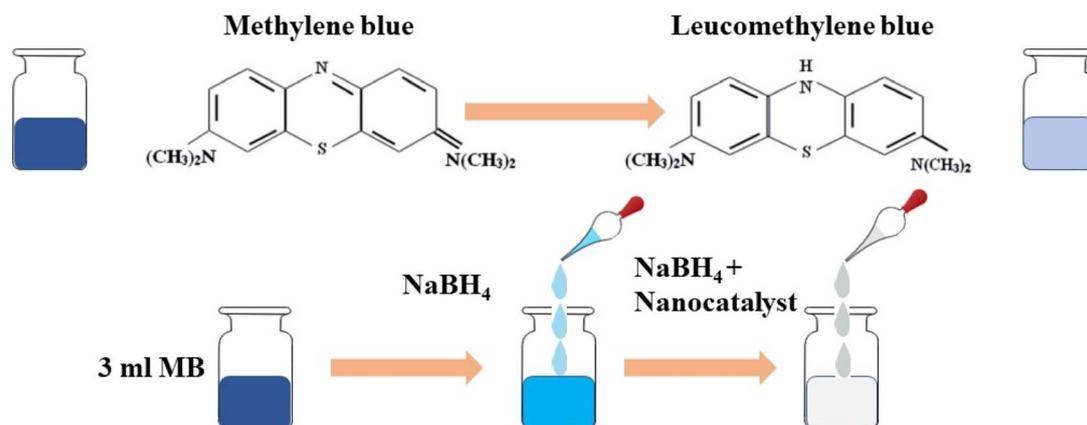

Fig. 2 Mechanism and experimental performance of catalytic activity.

concentration of deionized water (−ve control) was 50 μL. The plates were incubated at 37 °C for 24 hours. The inhibition zone measurements were carried out using a Vernier caliper.

2.4.5. Statistical analysis. The efficacy of the antimicrobial agents was assessed *via* size measurements, and the diameters of the inhibitory zones were then quantitatively evaluated *via* one-way analysis of variance (ANOVA) in SPSS 20.

2.5. Molecular docking analysis

The potential of targeting cell wall synthesis as an antibiotic strategy, and the role it plays in the bactericidal activity of certain NSs has been proposed. The discovery of new antibacterial drugs is heavily relies on the pivotal involvement of enzymes in the formation of peptidoglycan and nucleic acids. The suppression of bacterial cell walls results in their subsequent disintegration and cell death.[25-28] In this study, the inhibitory effects of Cs-Y_2O_3 NSs on DNA gyrase and MDR *E. coli* enzymes β-lactamase were evaluated. The crystal structures of DNA gyrase and β-lactamase enzymes from MDR *E. coli* were obtained from Protein Data Bank (PDB) under the accession codes 4KZ7 (with resolution of 1.72)[29] and 5MMP (resolution of 1.90),[30] respectively. With Sybyl X-2.0, the molecular docking

procedure was carried out,[31] using the sketch module to construct ligand structures. Additionally, PyMOL was used to visually visualize the binding interactions in three dimensions.[32]

3. Results and discussion

X-ray diffraction (XRD) was utilized to examine the crystal structure and crystallite size of pure and Cs-doped Y_2O_3 within the 2θ range of 20–60° as revealed in Fig. 3(a). Diffraction peaks detected at positions $2\theta = 28.8°$ (111), 30.4° ($40\bar{2}$), 32.2° (310), 33.1° ($11\bar{2}$), 34.6° (112), 37.1° ($\bar{4}11$), 42.6° (004), 54.7° ($71\bar{2}$) and 56.5° (711) were ascribed to monoclinic Y_2O_3 (m-Y_2O_3), (JCPDS: 00-044-0399/00-039-1063). The peaks appeared at $2\theta = 36.0°$ (411), 40.0° (332), and 55.0° (026), referring to cubic phase Y_2O_3 (JCPDS: 01-074-1828). A distinct peak is observed at an angle of 29.73° (100) attributed to 2 wt% incorporation of Cs. Similarly, a peak is observed at an angle of 50.11° (106) assigned to 4 wt% concentration of Cs. Furthermore, when the doping concentration of Cs is enhanced to 6 wt%, multiple peaks are observed at angles of 29.27° (004), 39.6° (104), 44.6° (105), 50.1° (106), 53.7° (112), and 56.0° (113). These peaks correspond to the hexagonal cesium yttrium oxide phase match with the JCPDS: 01-077-1611. In the 6% Cs-doped Y_2O_3 the extra peaks appeared at 29.5° (014) and 48.0° ($\bar{1}08$) were matched with JCPDS No. 00-021-1447, revealing a monoclinic structure of yttrium hydroxide. The average crystallite size in the range of 45–60 nm was assessed using the Scherrer formula.[33] The observed peak shifted towards lower 2θ values can be accredited to an increase in crystallite size as the dopant concentration increases and is also associated with the greater ionic radii (2.49 Å) of Cs.

Fourier transform infrared spectroscopy (FTIR) analysis conducted in the frequency range of 450–4000 cm^{-1} to investigate the chemical composition and functional groups analysis of pristine and Cs-doped Y_2O_3 can be represented in Fig. 3(b). The bands appeared at 500 and 550 cm^{-1} attributed to the metal oxygen band, as previously reported.[34] A Y-OH bond was attributed to the observed band at 950 cm^{-1}. The nanostructure exhibits a distinctive asymmetric stretching of Y–O–Y attributed to the band observed at 1060 cm^{-1}.[35] The observed spectral bands at around 1500 cm^{-1} ascribed to asymmetric stretching of the C–O bond and can be attributed to the absorption of CO_2 from the surrounding atmosphere. The spectral bands detected within the wavelength range of 3800–3350 cm^{-1} and at 1450 cm^{-1} are associated with OH stretching and bending vibration modes, respectively. The occurrence of this phenomenon can be accredited to the existence of hydroxyl groups and molecular water that are firmly adsorbed within the yttrium hydroxide crystal lattice.[34] The peak at 650 cm^{-1} with high intensity is credited to the stretching vibration of Y–O bonds, as reported earlier.[36]

Selected area electron diffraction (SAED) analysis revealed the presence of distinct bright circular rings that indicate the polycrystalline nature of synthesized Y_2O_3 and Cs-Y_2O_3 (Fig. 3(c–f)). These concentric rings show that the NSs have a high degree of crystallinity that matches XRD results.

UV-visible spectroscopy was employed to examine the absorption characteristic of the produced NSs in the spectral range of 250–600 nm, as represented in Fig. 4(a). The absorption spectrum of Y_2O_3 exhibits a prominent peak at 274 nm. The addition of (2, 4 and 6 wt%) Cs led to a noticeable shift in absorption towards longer wavelengths (redshift), suggesting a reduction in the bandgap energy (E_g) that is associated with the enhancement in the crystallite size.[37] The E_g was calculated using Tauc plot equation[38] (Fig. 4(b)). The direct E_g of pure NSs
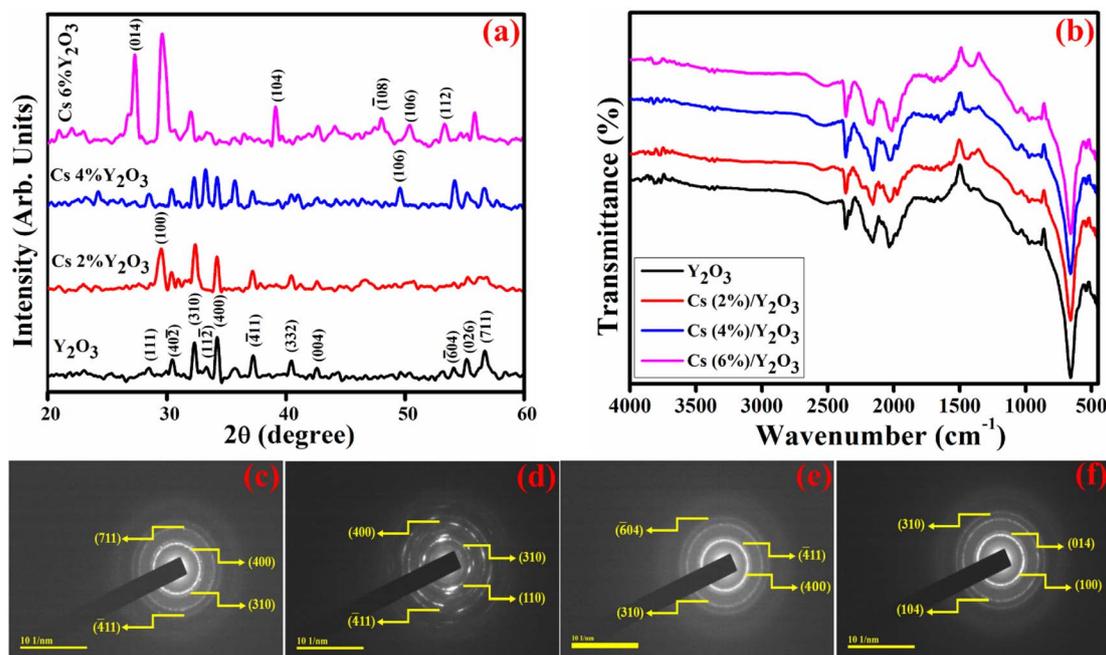

Fig. 3 (a) XRD analysis (b) FTIR analysis and (c–f) SAED micrograph of Y_2O_3, Cs (2, 4 and 6 wt%) doped Y_2O_3 NSs.
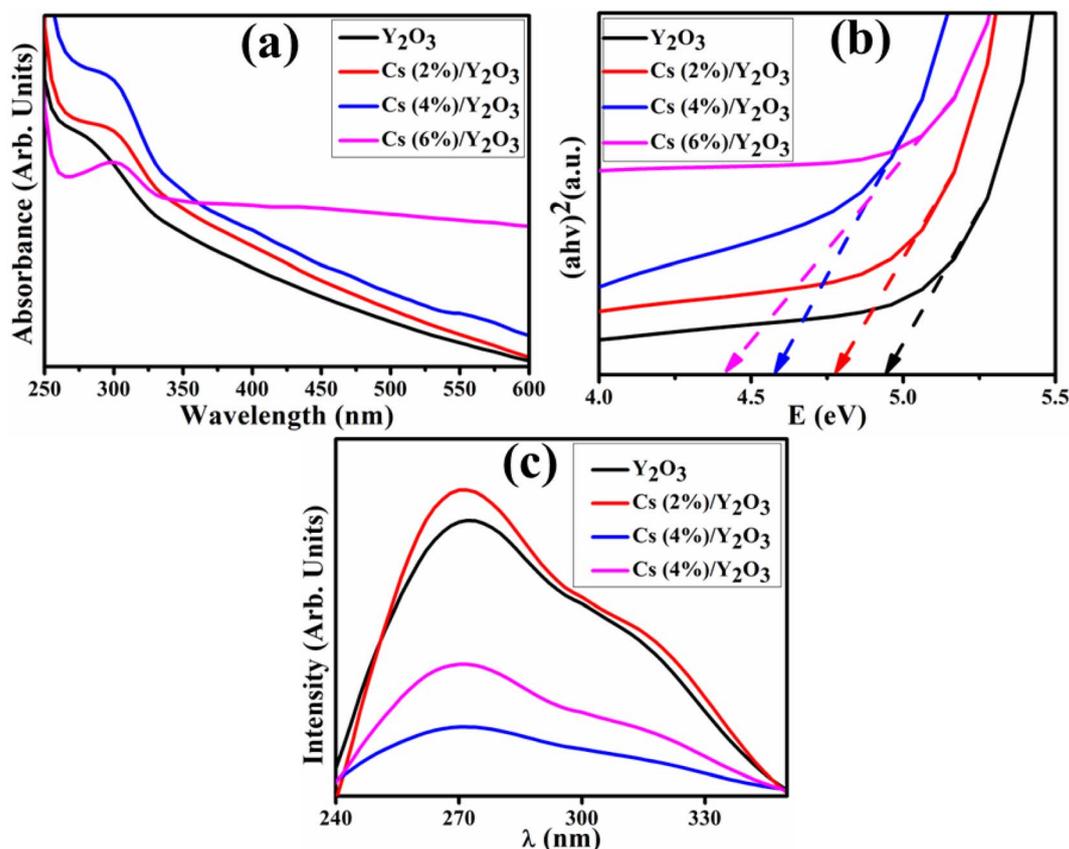
Fig. 4 (a) Absorption spectra, (b) band gap energy, and (c) emission spectra of Y_2O_3 and Cs (2, 4, and 6 wt%) doped Y_2O_3 NSs.

was determined as 4.94 eV. The addition of Cs in Y_2O_3 resulted in additional energy levels. There are only minor changes observed in the E_g of 2 wt% Cs-doped NSs. For instance, at higher concentrations of Cs, the E_g was approximately 4.41 eV. The decrease in E_g observed in doped samples can be attributed to the increase in crystallite size. This phenomenon may be attributed to the diminished orientation realignment and low crystallinity of the resultant materials.[39]

Photoluminescence (PL) spectroscopy emission spectra have been used to examine the mechanism of recombination and separation of electron and hole pairs of synthesized NSs can be depicted in Fig. 4(c). The excited electrons in valence band migrate to the conduction band at a specific excitation wavelength and then recombine to produce emission.[40] The Y_2O_3 NSs exhibit extensive emission peaks within the observable spectrum ranging from 260 to 290 nm. These emission peaks are mostly related to the presence of Y^{3+} ions observed at 274 nm. The decrease in peak intensity was attributed to the incorporation of Cs concentration, reflecting a greater potential for separating electron–hole pairs for photo-generated charge carriers. The increase in separation of photo-generated charge carriers exhibits maximum degradation of organic dye.

The chemical composition of pure and CS-Y_2O_3 NSs have been measured by energy-dispersive X-ray spectroscopy (EDS) analysis can be indicated in Fig. S1(a–d).† Prominent peaks corresponding to Y, O, and Cs were detected, providing

conclusive evidence of Cs into Y_2O_3 NSs. The presence of Au peaks may be accredited to the deposition of Au coating to reduce the charging effects.[41] The EDS mapping determines the elements involved in pure and CS-Y_2O_3 NSs with various color combinations (Fig. S1(e–h)†). The higher doped concentrations exhibited the dispersion of three components, Y, O, and Cs, confirming the synthesis of pristine and doped NSs.

Field emission scanning electron microscopy (FESEM) examines the surface morphology of synthesized Y_2O_3 and CS-Y_2O_3 NSs can be revealed in Fig. 5(a–d). Y_2O_3 indicates that particles are agglomerated particles and huge chunk was found can be seen in Fig. 5(a). The presence of a significant concentration of yttrium ions with Cs at varying percentages concentration of CS (2, 4, and 6 wt%) caused the initial homogenous nucleation can be disrupted. The active sites on the surface of Y_2O_3 aggregates would progressively increase in a specific direction as the reaction proceeds, and Y_2O_3 monomer concentration diminishes.[42] As the concentration of Cs increases, the surface of Y_2O_3 is distorted, and particles appear on the surface of cluster. The nanorods-like morphology with a rough surface appeared upon insertion of 6 wt% Cs.

The pictorial representation of transmission electron microscopy (TEM) was used to describe the internal structural morphology of Y_2O_3 and (2, 4, and 6 wt%) Cs-doped Y_2O_3 can be depicted in Fig. 6. Y_2O_3 revealed surface of atoms forming agglomerated nanocluster-like morphology. Incorporation of
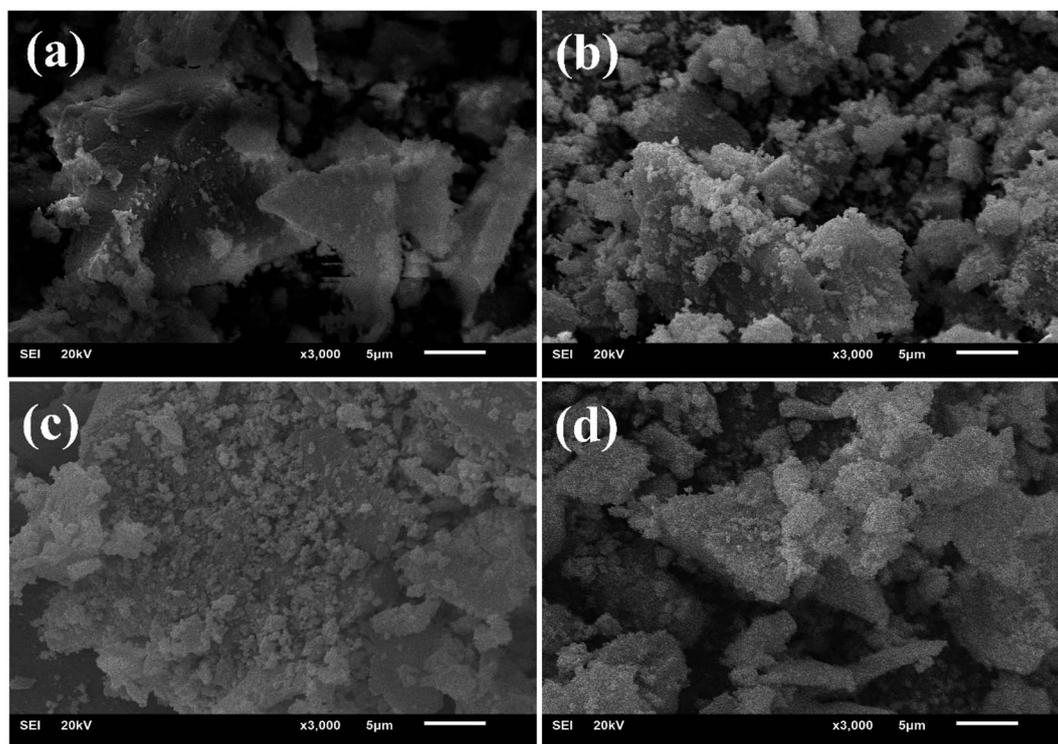
Fig. 5 (a–d) FESEM micrograph of pure and Cs (2, 4 and 6 wt%) doped Y_2O_3 NSs.
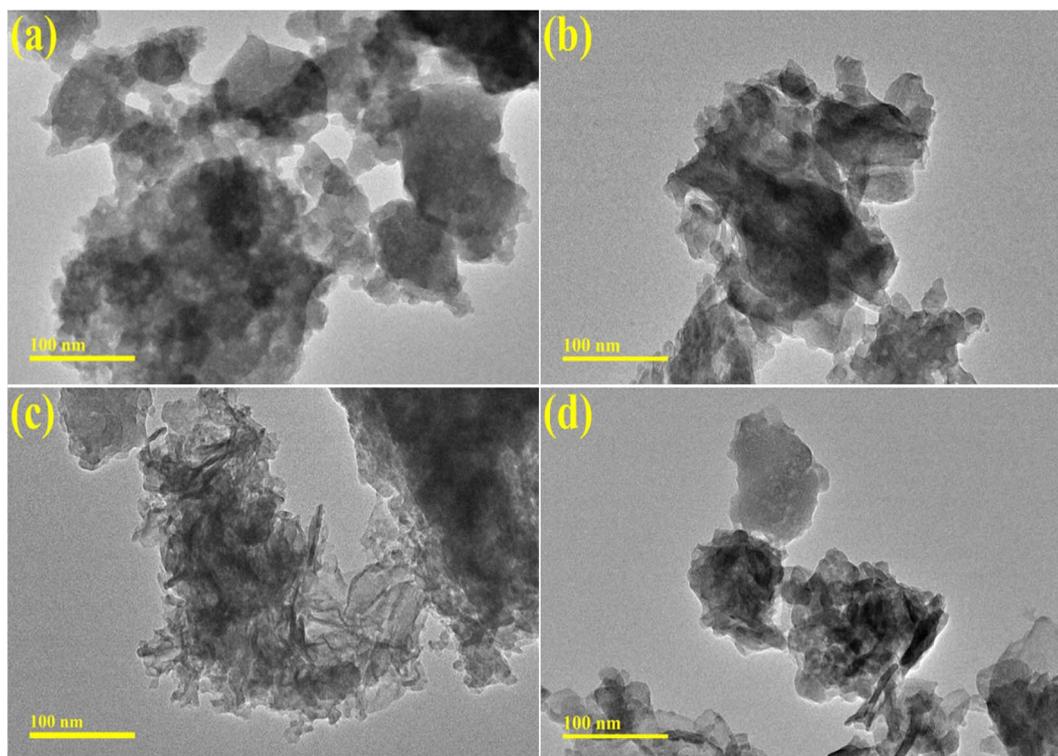

Fig. 6 TEM images (a) Y_2O_3 and (b–d) Cs (2, 4, and wt%)-doped Y_2O_3 NSs.

Cs, the morphology undergoes a transition to a dense nano-cluster morphology. 4 wt% doped exhibit Y_2O_3, the shape of generated nanocluster transforms a rod-like morphology. As the percentage concentration of Cs increases the agglomerated nanoparticles (NPs), a nanorod-like (NRs) morphology of Cs appeared on the surface of the nanocluster.
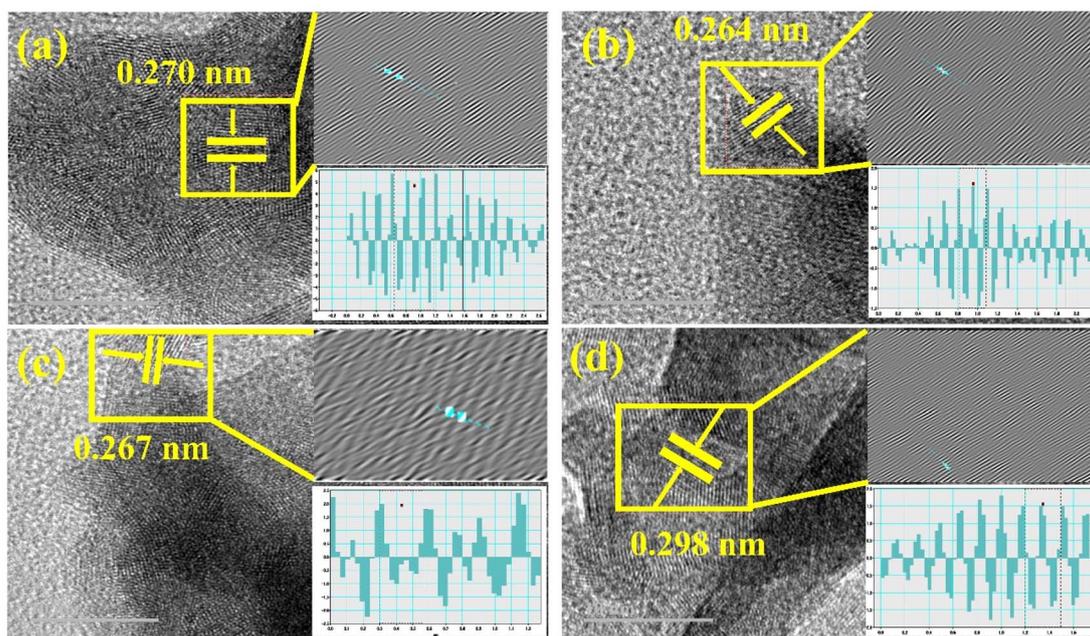
Fig. 7 (a–d) d-Spacing of Y_2O_3 and Cs (2, 4 and 6 wt%)-doped Y_2O_3 NSs.
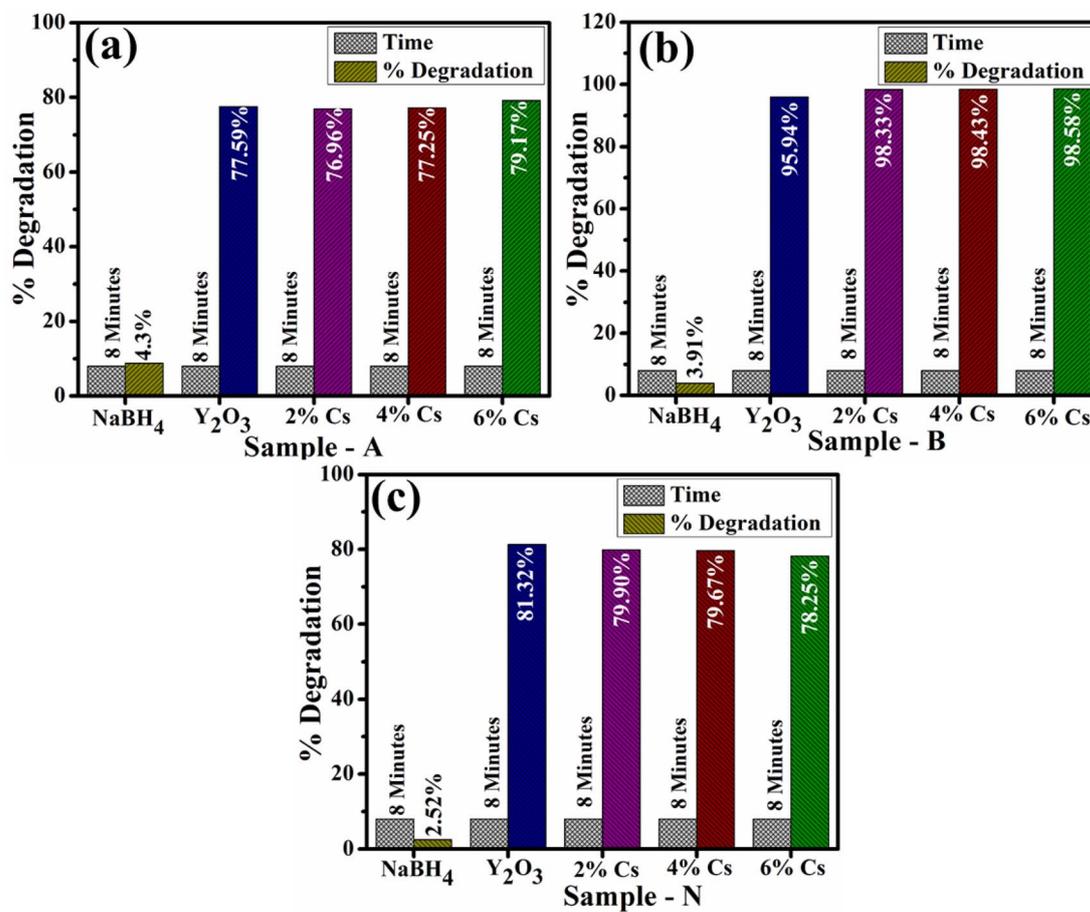

Fig. 8 Catalytic activity of Y_2O_3 and Cs-Y_2O_3 (2, 4, and 6 wt%) in (a) acidic, (b) basic and (c) neutral media.

Table 1 Antimicrobial activity of Y_2O_3 and Cs (2, 4 and 6 wt%)-doped Y_2O_3 NSs

Samples	Inhibition zone (mm)	
	0.5 mg/50 μL	1.0 mg/50 μL
Y_2O_3	1.65	2.50
2% Cs/Y_2O_3	2.25	3.05
4% Cs/Y_2O_3	2.90	3.45
6% Cs/Y_2O_3	3.15	4.15
Ciprofloxacin	5.0	5.0
DIW	0	0

Interlayer d-spacing of pure and (2, 4, 6 wt%) Cs-doped Y_2O_3 were measured as 0.270, 0.264, 0.267, and 0.298 nm, using high-resolution transmission electron microscopy (HRTEM) micrographs respectively indicated in Fig. 7. The measured interlayer d-spacing exhibit strong concurrence with the XRD results.

The catalytic activity of synthesized NSs was evaluated with the assistance of a reducing agent to degrade MB. The % age degradation was measured as 78.25–81.32% at pH ∼ 7 for a neutral medium, 76.96–79.17% for an acidic medium at pH ∼ 4, and 95.94–98.58% at pH ∼ 12 in a basic medium can be depicted in Fig. 8(a–c). As illustrated in Fig. 8, dye degradation without a catalyst attained the maximum of 4.3%, 3.91%, and 2.52% in 8 min in acidic, basic, and neutral environments, respectively. The pH is significantly important in determining the properties of dyes and mechanisms involve hydroxyl radicals and direct oxidation by H^+.[43] The pH value significantly affects the surface area and surface charge of the catalyst.[44] MB is a cationic dye that will adsorb onto a catalyst with a strong negative charge in a basic medium.[45] This leads to a higher degradation of organic dye attributed to a positive charge that enhanced electrostatic attraction between the catalyst surface and dye in the basic medium.

An acidic medium with a lower pH value leads to a positive charge on the catalyst surface and MB is also a cationic dye in consequence, there is no redox reaction taking place. The degradation of dye on the nanocatalyst surface decreases.[46] Using a doped nanocatalyst increased the percentage degradation in acidic and basic mediums. At higher concentrations of Cs, the catalytic activity for degradation of MB was increased. The dye degradation is affected by the crystallinity, shape, and surface area of synthesized NSs.[47,48]

The fundamental reaction steps comprise the catalytic reaction for the degradation of MB. The rate of reaction between MB and $NaBH_4$ was slow. The synthesized catalyst enhanced the reaction that acts as a relay between reactants. The catalyst helps speed up the electron transfer from BH_4^- ions to MB, leading to the formation of intermediate radicals, and it is most likely the complex mechanism that mediates the degradation of MB with $NaBH_4$. The redox reaction takes place between the reactants.[49] The degradation of MB in the existence of $NaBH_4$, and catalyst facilitates the transfer of electrons from the BH_4^- ions to the MB ions during dye degradation. The surface area and the number of active sites also play an effective role in degradation of dye molecules.[50,51] High catalytic efficiency is typically associated with a large surface area of catalyst. Further research is required to fully understand the degradation pathway, particularly the involvement of free radicals in the degradation process and subsequent intermediates.[52–55]

The *in vitro* antibacterial activity of Y_2O_3 and Cs (2, 4, and 6 wt%)-doped Y_2O_3 was assessed using an agar-based diffusion approach to measure inhibitory zones against Gram −ve bacteria, MDR *E. coli*. Many antibiotic studies use *E. coli* as a model organism since it is a relatively well-understood bacterium.[56] The inhibition zones were assessed between 1.65–3.15 mm and 2.50–4.15 mm, for low and high concentrations respectively. Additionally, ciprofloxacin exhibited an inhibition zone of 5.0 mm that acts as an efficient drug for microbial killing and DI water shows 0 mm can be depicted in Table 1. Moreover, Cs doped Y_2O_3 NSs effectively eliminated MDR *E. coli* bacteria. The Cs-doped Y_2O_3 exhibits enhanced bactericidal activity against MDR *E. coli*, compared to the findings obtained with pure.
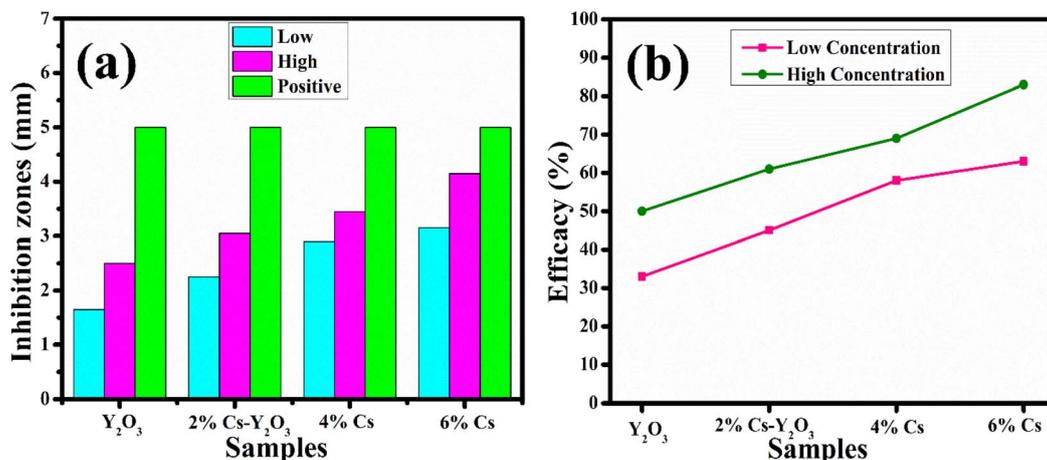

Fig. 9 Graphical representations of bactericidal activity of MDR *E. coli* (a) inhibition zones measurements and (b) % age efficacy at low concentrations and high concentrations.
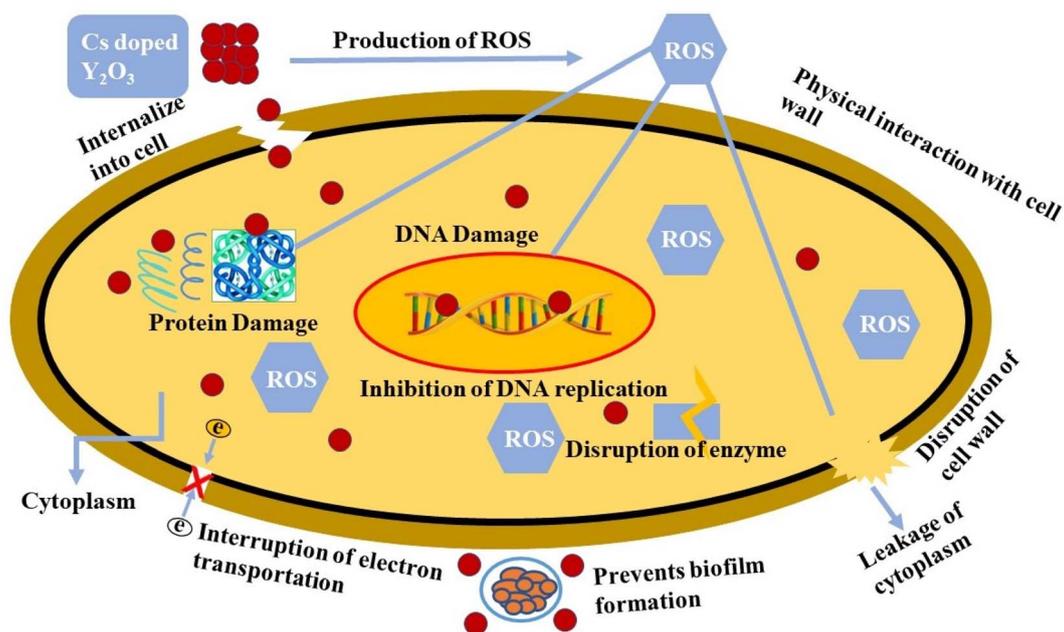
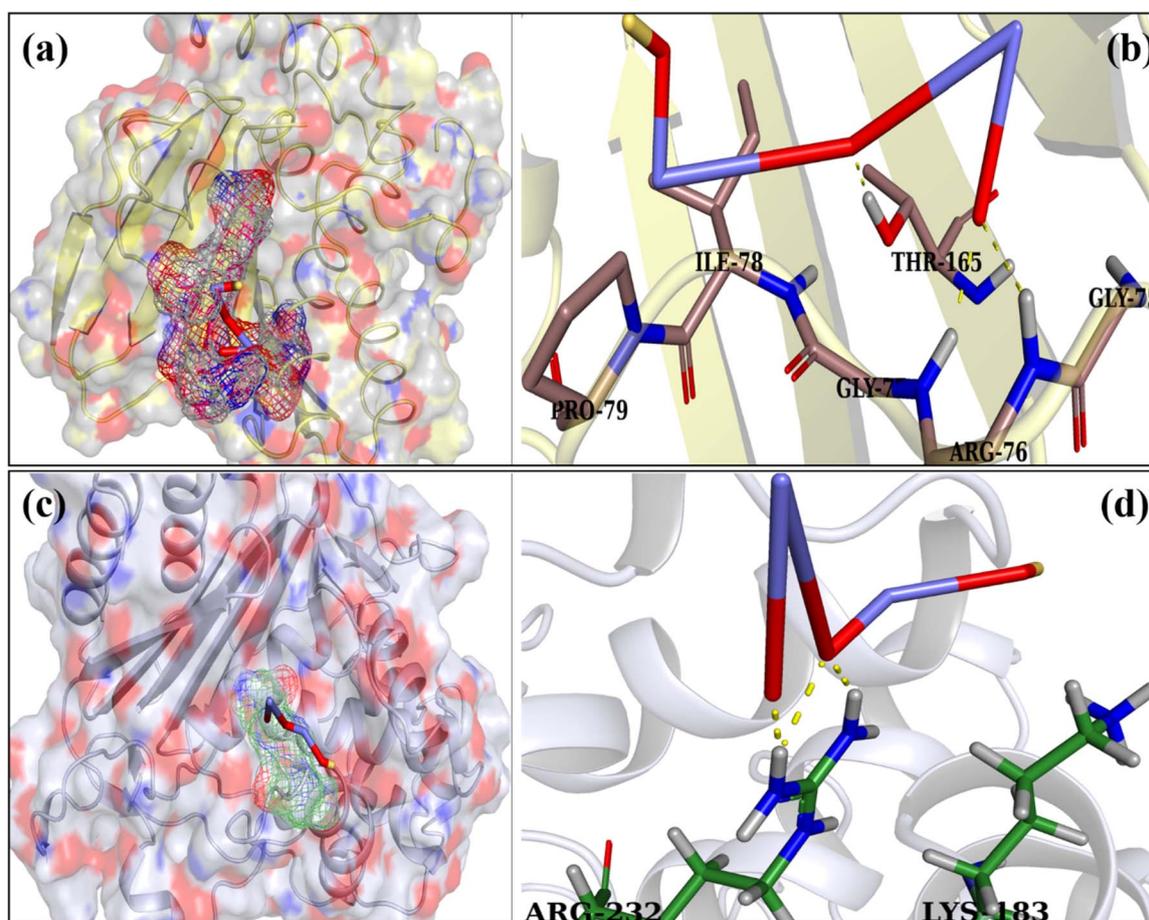**Fig. 10** Graphic illustration of antibacterial mechanism of prepared Cs-doped Y$_2$O$_3$ NSs.

Fig. 11 (a) Native ligand binding inside active pocket of DNA gyrase *E. coli* (superimposed), (b). Cs-Y$_2$O$_3$ DNA gyrase *E. coli* complex. (c) Ligand binding inside active pocket of β-lactamase *E. coli*, (d). Cs-Y$_2$O$_3$ β-lactamase *E. coli* complex.

© 2024 The Author(s). Published by the Royal Society of Chemistry

Efficacy (%) was determined by dividing the inhibition zone of the synthesized sample by the inhibition zone of ciprofloxacin, represented in Fig. 9. The measured efficiency for low concentration is 33%, 45%, 58%, and 63% and for high concentration 50%, 61%, 69%, and 83% respectively pure and doped NSs.

Through interactions with the bacteria cell membrane, Y_2O_3 NSs produce toxicity and lead to bacterial cell death. Due to the robust electrostatic forces, Y_2O_3 nanoparticles have a notable affinity for the bacterial cell membrane, enabling them to efficiently constrain the growth of both Gram +ve and Gram −ve bacteria. Based on earlier reports on the formation pathways of Y_2O_3 nanoparticles, it has been observed that yttrium ions can permeate the cell wall of bacteria. This penetration leads to the inhibition of bacterial growth by down-regulating enzyme activity, ultimately causing the death of bacterial cells.[35,57–59] The schematic diagram of doped nanocatalyst used during the antibacterial process (Fig. 10).

Recent studies have shown the importance of cell wall production (peptidoglycan synthesis) and the pathway different NSs use for nucleic acid biosynthesis for antibacterial activity. However, the exact mechanism still needs to be clarified. Fig. 11(a) illustrates the binding affinity of Cs-Y_2O_3 NSs within the active site of DNA gyrase in MDR *E. coli*. The Cs-Y_2O_3 NSs exhibited favorable binding score of 3.02, indicating the presence of hydrogen bonding with crucial amino acid residues Thr165, Gly75, Arg76, Pro79, and Gly77 (Fig. 11(b)). Additionally, the propensity of Cs-Y_2O_3 NSs to interact with beta-lactamase *E. coli* were examined (Fig. 11(c)) with binding scores of 2.01 for the proposed molecule in well-docked conformations. The interaction of Cs-Y_2O_3 NSs between Arg232 and Lys183 was observed (Fig. 11(d)).

Cs-Y_2O_3 NSs were shown to have binding affinity for β-lactamase and DNA gyrase, suggesting them effective inhibitors of these enzymes.

4. Conclusion

In this research work, Y_2O_3 and Cs-doped Y_2O_3 were successfully synthesized using a cost-effective co-precipitation approach. The XRD analysis of the prepared samples confirmed the monoclinic and cubic phase structure of NSs. Incorporating Cs led to a significant increase in crystallite size (45–60 nm). Cs doping resulted in a subtle redshift in the absorption edge, primarily due to contamination in bandgap states. The TEM analysis of Y_2O_3 revealed the presence of a nanoparticle and nanorod-like morphology. Cs-doped Y_2O_3 NSs significantly enhanced catalytic efficiency by up to 99%. The maximum efficacy (83%) was observed at 6% incorporation of Cs, revealing the death of MDR *E. coli*. *In silico* molecular docking investigations indicated that the inhibition of DNA gyrase and β-lactamase as probable mechanisms explaining the bactericidal action of Cs-Y_2O_3 NSs. This scientific approach of Cs doping resulted in higher catalytic efficiency, whereas *in silico* studies reveal molecular insights into antibacterial action. These findings offer promising avenues for developing efficient and multifunctional nanomaterials by analyzing the role of Cs doping in improving the catalytic and antimicrobial performance of Y_2O_3 NSs.

Data availability

The data used in this manuscript can be available on proper demand.

Conflicts of interest

The authors declare no known conflict of interest.

Acknowledgements

References

1 R. Rajkumar, G. Ezhumalai and M. Gnanadesigan, *Environ. Technol. Innovation*, 2021, **21**, 101282.

2 M. M. Hasan, M. A. Shenashen, M. N. Hasan, H. Znad, M. S. Salman and M. R. Awual, *J. Mol. Liq.*, 2021, **323**, 114587.

3 A. Raza, M. Ikram, M. Aqeel, M. Imran, A. Ul-Hamid, K. N. Riaz and S. Ali, *Appl. Nanosci.*, 2020, **10**, 1535–1544.

4 R. Connor, *The United Nations World Water Development Report 2015: Water for a Sustainable World*, UNESCO publishing, 2015.

5 N. Sivarajasekar and R. Baskar, *J. Ind. Eng. Chem.*, 2014, **20**, 2699–2709.

6 Y. Hua, J. Xiao, Q. Zhang, C. Cui and C. Wang, *Nanoscale Res. Lett.*, 2018, **13**, 99.

7 X. Liu, Y. Wang, B. Zhu, C. Xie, Y. Sun and H. Yang, *Mater. Res. Express*, 2019, **6**, 106591.

8 M. S. Samuel, S. S. Shah, V. Subramaniyan, T. Qureshi, J. Bhattacharya and N. D. Pradeep Singh, *Int. J. Biol. Macromol.*, 2018, **119**, 540–547.

9 M. S. Samuel, M. E. A. Abigail and C. Ramalingam, *PLoS One*, 2015, **10**, e0118999.

10 F. S. Omar, H. Nay Ming, S. M. Hafiz and L. H. Ngee, *Int. J. Photoenergy*, 2014, **2014**, 176835.

11 N. Rosman, W. N. W. Salleh, M. A. Mohamed, J. Jaafar, A. F. Ismail and Z. Harun, *J. Colloid Interface Sci.*, 2018, **532**, 236–260.

12 G. Wang, Q. Peng and Y. Li, *Acc. Chem. Res.*, 2011, **44**, 322–332.

13 Y. Li, G. Wang, K. Pan, Y. Qu, S. Liu and L. Feng, *Dalton Trans.*, 2013, **42**, 3366–3372.

14 S. V. Eliseeva and J.-C. G. Bünzli, *Chem. Soc. Rev.*, 2010, **39**, 189–227.

15 R. Bomila, S. Srinivasan, S. Gunasekaran and A. Manikandan, *J. Supercond. Novel Magn.*, 2018, **31**, 855–864.

16 Q.-L. Yao, M. He, Y.-R. Kong, T. Gui and Z.-H. Lu, *Rare Met.*, 2023, **42**, 3410–3419.

17 R.-B. Zhang, Z.-A. Tu, S. Meng, G. Feng, Z.-H. Lu, Y.-Z. Yu, T. R. Reina, F.-Y. Hu, X.-H. Chen and R.-P. Ye, *Rare Met.*, 2023, **42**, 176–188.

18 C.-C. Li, M.-W. Zhang, J.-W. Xin, L. Wei and W.-Y. Zhao, *Rare Met.*, 2024, **43**, 1758–1768.

19 R. Srinivasan, R. Yogamalar, A. Vinu, K. Ariga and A. C. Bose, *J. Nanosci. Nanotechnol.*, 2009, **9**, 6747–6752.

20 H. Choi, J. Jeong, H.-B. Kim, S. Kim, B. Walker, G.-H. Kim and J. Y. Kim, *Nano Energy*, 2014, **7**, 80–85.

21 J. G. Holt, N. R. Krieg, P. H. Sneath, J. T. Staley and S. T. Williams, *Bergey's Manual of Determinate Bacteriology*, 1994.

22 A. W. Bauer, W. M. Kirby, J. C. Sherris and M. Turck, *Am. J. Clin. Pathol.*, 1966, **45**, 493–496.

23 F. Adzitey, S. Yussif, R. Ayamga, S. Zuberu, F. Addy, G. Adu-Bonsu, N. Huda and R. Kobun, *Microorganisms*, 2022, **10**, 1335.

24 B. A. Iwalokun, A. Ogunledun, D. O. Ogbolu, S. B. Bamiro and J. Jimi-Omojola, *J. Med. Food*, 2004, **7**, 327–333.

25 D. Lim and N. C. J. Strynadka, *Nat. Struct. Biol.*, 2002, **9**, 870–876.

26 J. Buxeraud and S. Faure, *Actual. Pharm.*, 2016, **55**, 1–5.

27 M. M. Mullis, I. M. Rambo, B. J. Baker and B. K. Reese, *Front. Microbiol.*, 2019, **10**, 2518.

28 I. Shahzadi, M. Islam, H. Saeed, A. Haider, A. Shahzadi, J. Haider, N. Ahmed, A. Ul-Hamid, W. Nabgan, M. Ikram and H. A. Rathore, *Int. J. Biol. Macromol.*, 2022, **220**, 1277–1286.

29 S. Barelier, O. Eidam, I. Fish, J. Hollander, F. Figaroa, R. Nachane, J. J. Irwin, B. K. Shoichet and G. Siegal, *ACS Chem. Biol.*, 2014, **9**, 1528–1535.

30 P. Panchaud, T. Bruyère, A.-C. Blumstein, D. Bur, A. Chambovey, E. A. Ertel, M. Gude, C. Hubschwerlen, L. Jacob, T. Kimmerlin, T. Pfeifer, L. Prade, P. Seiler, D. Ritz and G. Rueedi, *J. Med. Chem.*, 2017, **60**, 3755–3775.

31 I. Shahzadi, M. Islam, H. Saeed, A. Shahzadi, J. Haider, A. Haider, M. Imran, H. A. Rathore, A. Ul-Hamid, W. Nabgan and M. Ikram, *Int. J. Biol. Macromol.*, 2023, **235**, 123874.

32 I. Shahzadi, M. Aqeel, A. Haider, S. Naz, M. Imran, W. Nabgan, A. Al-Shanini, A. Shahzadi, T. Alshahrani and M. Ikram, *ACS Omega*, 2023, **8**, 30681–30693.

33 O. M. Lemine, *Superlattices Microstruct.*, 2009, **45**, 576–582.

34 K.-J. Jeong and D.-S. Bae, *Korean J. Mater. Res.*, 2012, **22**, 78–81.

35 S. K. Kannan and M. Sundrarajan, *Bull. Mater. Sci.*, 2015, **38**, 945–950.

36 C. A. Traina and J. Schwartz, *Langmuir*, 2007, **23**, 9158–9161.

37 R. Srinivasan, R. Yogamalar and A. C. Bose, *Mater. Res. Bull.*, 2010, **45**, 1165–1170.

38 P. Makuła, M. Pacia and W. Macyk, *J. Phys. Chem. Lett.*, 2018, **9**, 6814–6817.

39 Y. Hanifehpour, M. Abdolmaleki and S. W. Joo, *Inorganics*, 2021, **9**, 88.

40 A. Erbe, S. Nayak, Y. H. Chen, F. Niu, M. Pander, S. Tecklenburg and C. Toparli, in *Encyclopedia of Interfacial Chemistry*, ed. K. Wandelt, Elsevier, Oxford, 2018, pp. 199–219, DOI: 10.1016/B978-0-12-409547-2.14061-2.

41 J. B. Park, Y.-J. Kim, S.-M. Kim, J. M. Yoo, Y. Kim, R. Gorbachev, I. I. Barbolina, S. J. Kim, S. Kang, M.-H. Yoon, S.-P. Cho, K. S. Novoselov and B. H. Hong, *2D Mater.*, 2016, **3**, 045004.

42 G. Bhavani and S. Ganesan, *Int. J. Phys.*, 2012, **1**, 32–40.

43 A. Alkaim, A. Aljeboree, N. Alrazaq, S. Baqir, F. Hussein and A. Lilo, *Asian J. Chem.*, 2014, **26**, 8445.

44 R. K. Singh, S. S. Behera, K. R. Singh, S. Mishra, B. Panigrahi, T. R. Sahoo, P. K. Parhi and D. Mandal, *J. Photochem. Photobiol., A*, 2020, **400**, 112704.

45 F. Azeez, E. Al-Hetlani, M. Arafa, Y. Abdelmonem, A. A. Nazeer, M. O. Amin and M. Madkour, *Sci. Rep.*, 2018, **8**, 7104.

46 I. Khan, K. Saeed, I. Zekker, B. Zhang, A. H. Hendi, A. Ahmad, S. Ahmad, N. Zada, H. Ahmad, L. A. Shah, T. Shah and I. Khan, *Water*, 2022, **14**, 242.

47 A. Shahpal, M. Aziz Choudhary and Z. Ahmad, *Cogent Chem.*, 2017, **3**, 1301241.

48 M. Rashid, M. Ikram, A. Haider, S. Naz, J. Haider, A. Ul-Hamid, A. Shahzadi and M. Aqeel, *Dalton Trans.*, 2020, **49**, 8314–8330.

49 S. Muhammad, U. Muhammad and H. Atta ul, in *Photochemistry and Photophysics*, ed. S. Satyen and M. Sankalan, IntechOpen, Rijeka, 2018, ch. 11, DOI: 10.5772/intechopen.75008.

50 M. Ikram, T. Inayat, A. Haider, A. Ul-Hamid, J. Haider, W. Nabgan, A. Saeed, A. Shahbaz, S. Hayat, K. Ul-Ain and A. R. Butt, *Nanoscale Res. Lett.*, 2021, **16**, 56.

51 A. A. Fairuzi, N. N. Bonnia, R. M. Akhir, M. A. Abrani and H. M. Akil, *IOP Conf. Ser.: Earth Environ. Sci.*, 2018, **105**, 012018.

52 W. Shen, X. Dong, Y. Zhu, H. Chen and J. Shi, *Microporous Mesoporous Mater.*, 2005, **85**, 157–162.

53 M.-F. Luo, Y.-P. Song, J.-Q. Lu, X.-Y. Wang and Z.-Y. Pu, *J. Phys. Chem. C*, 2007, **111**, 12686–12692.

54 W. Li, F. Wang, Y. Shi and L. Yu, *Chin. Chem. Lett.*, 2023, **34**, 107505.

55 Y. Chen, C. Chen, Y. Liu and L. Yu, *Chin. Chem. Lett.*, 2023, **34**, 108489.

56 K. Kandasamy and P. Kumpati, *J. Appl. Biol. Biotechnol.*, 2023, **11**, 112–118.

57 N. J. Bassous, C. B. Garcia and T. J. Webster, *ACS Biomater. Sci. Eng.*, 2021, **7**, 1787–1807.

58 C. Maria Magdalane, K. Kaviyarasu, J. Judith Vijaya, B. Siddhardha and B. Jeyaraj, *J. Photochem. Photobiol., B*, 2017, **173**, 23–34.

59 X. Chen, S. Zhuang, W. Yan, Z. Zeng, J. Feng, H. Cao and L. Yu, *Chin. Chem. Lett.*, 2024, **35**, 109635.